AGU PUBLICATIONS

JGR

Journal of Geophysical Research: Oceans

RESEARCH ARTICLE

10.1002/2015JC011255

The modulation of the seasonal cross-shelf sea level variation by the cold pool in the Middle Atlantic Bight

Jin Sha[1], Young-Heon Jo[1,2], Xiao-Hai Yan[1,3], and W. T. Liu[4]

[1]College of Earth, Ocean, and Environment, University of Delaware, Newark, Delaware, USA, [2]Now at Department of Oceanography, Pusan National University, Busan, South Korea, [3]University of Delaware and Xiamen University, Joint Institute of Coastal Research and Management, Newark, Delaware, USA, [4]Jet Propulsion Laboratory, California Institute of Technology, Pasadena, California, USA

Key Points:
- The 20 year averaged temperature and thermal steric height show the cold pool feature
- The thermal steric height explains 87% annual variations of the altimetry SLA along the transect
- The multiyear locations of reconstructed SLA depression agree with the in situ cold pool locations

Correspondence to:
X.-H. Yan,
xiaohai@udel.edu

Citation:
Sha, J., Y.-H. Jo, X.-H. Yan, and W. T. Liu (2015), The modulation of the seasonal cross-shelf sea level variation by the cold pool in the Middle Atlantic Bight, *J. Geophys. Res. Oceans*, *120*, 7182–7194, doi:10.1002/2015JC011255.

Received 20 AUG 2015
Accepted 5 OCT 2015
Accepted article online 15 OCT 2015
Published online 6 NOV 2015

Abstract This study explores the influence of the cold pool in the Middle Atlantic Bight (MAB) to cross-shelf sea surface slope by fitting an annual harmonic to temperature and salinity profiles from 1993 to 2012 and compares to the 20 year averaged altimetry sea level anomaly (SLA). The consistency within the bottom temperature, thermal steric height, total steric height, and altimetry observation validates that the cold pool induces a depressed sea level in the middle shelf overlapping with the dominant surface seasonal cycles. Temporally, the cold pool pattern is most apparent in July and August as a result of magnitude competition between the thermal and haline steric height. In addition, Ensemble Empirical Mode Decomposition (EEMD) is employed to reconstruct the altimetry SLA and reveals the middle-shelf depression pattern from single year's SLA data. The locations of the SLA depression from 1993 to 2012 agree with the cold pool locations identified from in situ measurements, suggesting a promising application of altimetry SLA in the cold pool study. Conclusively, this study reveals the modulation of the cross-shelf sea level variation by the cold pool, and contributes to the understanding of the sea level response to water masses on the continental shelf.

1. Introduction

The Middle Atlantic Bight (MAB) cold pool refers to a cold bottom water mass ($<10^{\circ}$C) located in the MAB, which is one of the primary water masses of this region [*Fairbanks*, 1982]. The cold pool was first recorded as a cold belt extending from 30 to 80 m isobath with varying temperature and spatial coverage year by year [*Bigelow*, 1933]. The cold winter water persists at the bottom in spring, becomes increasingly isolated from the surface warm water in summer, and disappears during the fall [*Ketchum and Corwin*, 1964; *Houghton et al*., 1982]. The cold pool locates on the middle and outer shelf, differing from tidal and wind mixing inshore water and the warmer saltier offshore slope water [*Fairbanks*, 1982; *Houghton et al*., 1982; *Churchill and Gawarkiewicz*, 2014]. The location of the cold pool in the alongshore direction is related to the cross-shelf section area [*Houghton et al*., 1982]. The cold pool is part of a longer equatorward along-shelf coastal current system originating from Greenland/Labrador shelf [*Chapman et al*., 1986; *Chapman and Beardsley*, 1989]. The cold pool has biological influences on the population dynamics of the phytoplankton, fish juvenile abundance, and the distribution of MAB benthic and demersal biota [*Malone et al*., 1983; *Sullivan et al*., 2005; *Narváez et al*., 2014]. The cold pool water enters into the southern MAB, shifts offshore entrained by the Gulf Stream, playing an important role in the chlorophyll transport along the shelf and the carbon budget of the North Atlantic [*Wood et al*., 1996; *Bignami and Hopkins*, 2003; *Churchill and Gawarkiewicz*, 2014].

Previous studies on the cold pool were based on the in situ measurements and model results. However, the sparse nature of in situ measurements limited further investigation of the cold pool because no continuous time series are available. Moreover, remote sensing data with large spatial coverage and long time series were seldom used in the cold pool study because the cold pool water locates under the thermocline. However, recent studies revealed the possibility of studying subsurface processes with surface variables retrieved from satellite data [*Klemas and Yan*, 2014], such as the application of sea level anomaly (SLA) from altimeter on Mediterranean Eddies tracking [*Yan et al*., 2006; *Ienna et al*., 2014], by removing surface layer steric components from SLA. Based on previous studies of the steric height [*Gill and Niller*, 1973], the cold pool with lower than ambient temperature generates the depressed thermal steric height and thus induces

depressed sea level anomaly. The cold pool can possibly have surface expressions in the sea level anomaly observation. It is necessary to investigate the relationship between the cold pool and altimetry SLA, not only for a baseline of cold pool studies utilizing remote sensing data, but also for a better understanding of the response of the sea level variations to mesoscale features on the continental shelf.

This paper focused on how the cold pool feature in the thermal and haline annual cycles influence the cross-shelf SLA. We organized this paper as follows. First, we applied single annual harmonic fitting to obtain the 20 year mean annual cycles containing the cold pool feature from in situ measurements. Second, different steric components are derived from the measurements and compared. Finally, attempts were made to extract seasonal components from altimetry SLA data to reveal the cold pool pattern, and the locations of SLA depression are compared to the bottom temperature.

2. Data and Methods

2.1. Data

Temperature and salinity profiles of Conductivity-Temperature-Depth (CTD), Profiling Floats (PFL), Expendable Bathythermograph (XBT), and Mechanical Bathythermographs (MBT) are collected from World Ocean Database (WOD/NOAA) during 1993–2012 in MAB. CTD and PFL measurements have coupled temperature and salinity (TS) profiles and are used in the derivation of the steric components [*Gill and Niller*, 1973]. Most measurements within 1000 m isobath come from CTD. XBT and MBT do not provide salinity profiles and thus are used in the cold pool location determination together with CTD and PFL. Following criteria are applied at each location to make sure the profiles are "acceptable" (as of *Lentz* [2003]): more than five samples are available within one vertical profile; the measured temperature values are within -2°C to 35°C; salinity values are within 0–40; the deepest samples do not exceed the water depth by 10 m. A subset of 24,225 TS couples are available from a total of 26,702 within MAB (35°N–42°N, 76°W–68°W).

We use the gridded Sea Level Anomaly (SLA), which is one of Ssalto/Duacs multimission altimeter products released on 15 April 2014 by AVISO. This data set contains daily maps from 1993 to 2012 on a 1/4° Cartesian grid referring to a 20 year mean (1993–2012) with tidal and inverse barometer corrections. All data points within 25 km from the coastline, though shown as part of our figures, should be excluded or analyzed with caution to avoid the contamination from land. The along-track SLA measurements (e.g., track 50 of Jason 1 and 2) are also available from AVISO but are not used in this study based on the concerns mentioned in section 2.2. The daily gridded SLA was first interpolated to a transect, as described in section 2.2, so that we got the daily time series of SLA over a transect line. Moreover, the daily time series were averaged over 20 years for each month resulting in a monthly climatology or the mean annual cycle of SLA.

2.2. Cross-Shelf Transect and Harmonic Fitting

Previous literature sources reveal that the cold pool persists from late spring to early fall. By composing all available bottom temperatures of CTD and PFL from April to September during the past two decades (1993–2012), we obtained the "footprint" of the cold pool with bottom temperature <10°C (Figure 1a). In the cross-shelf direction, the cold pool locates within 100 m isobath over the middle and outer shelf. In this study, we follow the definition of *Csanady* [1982] that the middle shelf is around 48 m isobath and outer shelf is around 96 m isobath. In the along-shelf direction, the cold pool distributes from Nantucket Shoals in the northeast to Cape Hatteras in the southwest with the coldest core locating around the Hudson Valley (Figure 1b). We made a cross-shelf transect to investigate the influence of the cold pool on the cross-shelf sea surface height. The transect location is chosen based on several concerns: the transect is made into the cold core of the cold pool to obtain the largest temperature gradient; the transect is outside the Hudson Valley to avoid possible anomalous features [*Lentz et al*., 2014]. This transect has an offshore resolution of 15 km and a vertical resolution of 1 m (by linear interpolation). The interval of 15 km was chosen to make sure the cold pool feature could be fully described but without a data gap. Ambient area within alongshore distance of 20 km from the transect (grey rectangle in Figure 1a) is also included to reduce the uncertainty of the sparse measurements. As we essentially focus on the annual cycles, single annual harmonic fitting [*Lentz*, 2008] is applied to estimate the annual cycle at each location. The fitted data time series are described as

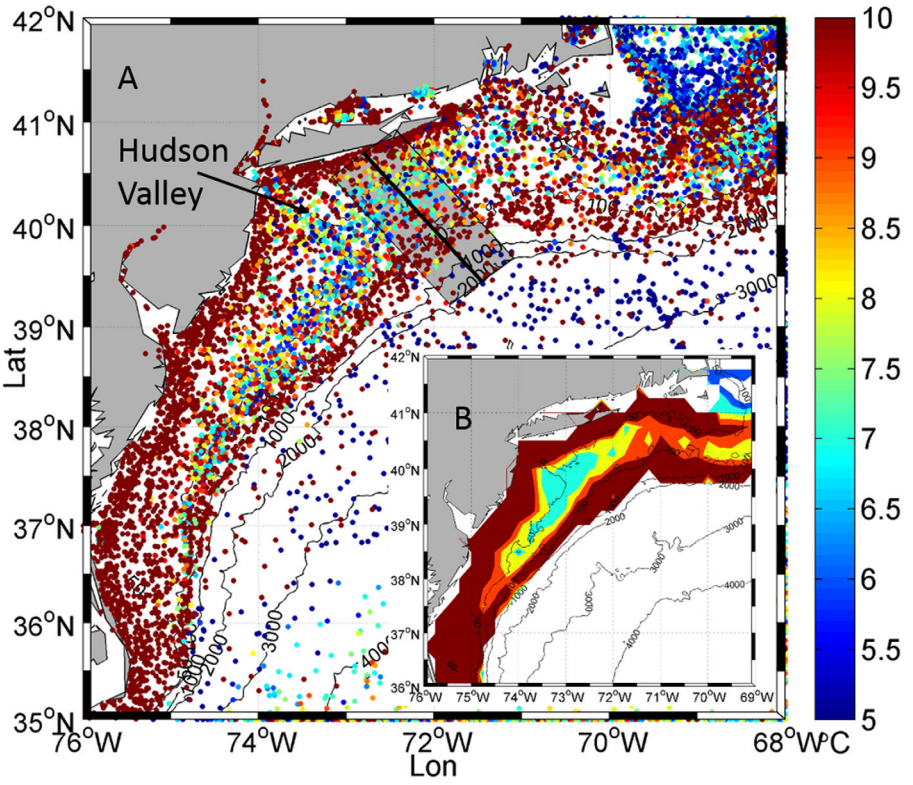

Figure 1. Cold pool spatial distribution. (a) The scattered bottom temperatures from CTD and PFL profiles from May to September during 1993–2012. The black line in the grey rectangle is the cross-shelf transect, averaging over the shadowed rectangle. (b) The contour of the bottom temperatures on the shelf indicating the location of the cold pool (with temperature <10°C).

$$y = a + bt + c\sin(\omega t) + d\cos(\omega t) \tag{1}$$

where t is time and ω is the annual frequency. Using available CTD and PFL measurements as y, the coefficients of a, b, c, d are determined based on the least square theorem. The term $a+bt$ denotes the linear trend, and $c\sin(\omega t)+d\sin(\omega t)$ denotes the annual cycle. The value of b is on the order of 10^{-4}°C/d being consistent with the estimation of *Forsyth et al.* [2015]. The root-mean-squared deviation/error (RMSE) and the correlation coefficient R between the fitted and measured values were assessed (Figure 2). For the middle shelf within 90 km offshore distance, the RMSEs are less than 2°C with $R>0.8$ ($p<0.05$). The fitted annual cycle explains more than 64% of the temperature variations. Concerning the linear trend term in equation (1), approximations of different orders (using only the mean a, the first-order approximation $a+bt$, and the second-order approximation $a+bt+ct^2$) were tested. The domain-averaged RMSE using the first-order approximation is 0.06°C lower than using the mean while being 0.01°C higher than using the second-order approximation. We used $a+bt$ as the linear trend approximation as a balance between the computational expenses and the accuracy. The data were finally averaged over 20 years to obtain the mean annual cycle. These steps are applied to TS profiles and the corresponding steric components.

2.3. Ensemble Empirical Mode Decomposition

We applied Ensemble Empirical Mode Decomposition (EEMD) [*Wu and Huang*, 2009; *Wu et al.*, 2009] to decompose the gridded SLA. The original Empirical Mode Decomposition (EMD) [*Huang et al.*, 1998] is a useful tool for the nonlinear, nonstationary time series, separating the data set into a finite number of intrinsic mode functions (IMFs). The method identifies different oscillation cycles based on their characteristic temporal scales. The number of IMFs is determined by the length of the data set. EEMD [*Wu and Huang*, 2009] is an improved approach by adding white noise into the data and treating the mean of a sufficient number of trials as the final result. EEMD is believed to eliminate the mode-mixing problem of the original EMD algorithm. In this study, we used EEMD to extract the annual cycles (with above 90% significance level) of SLA data.

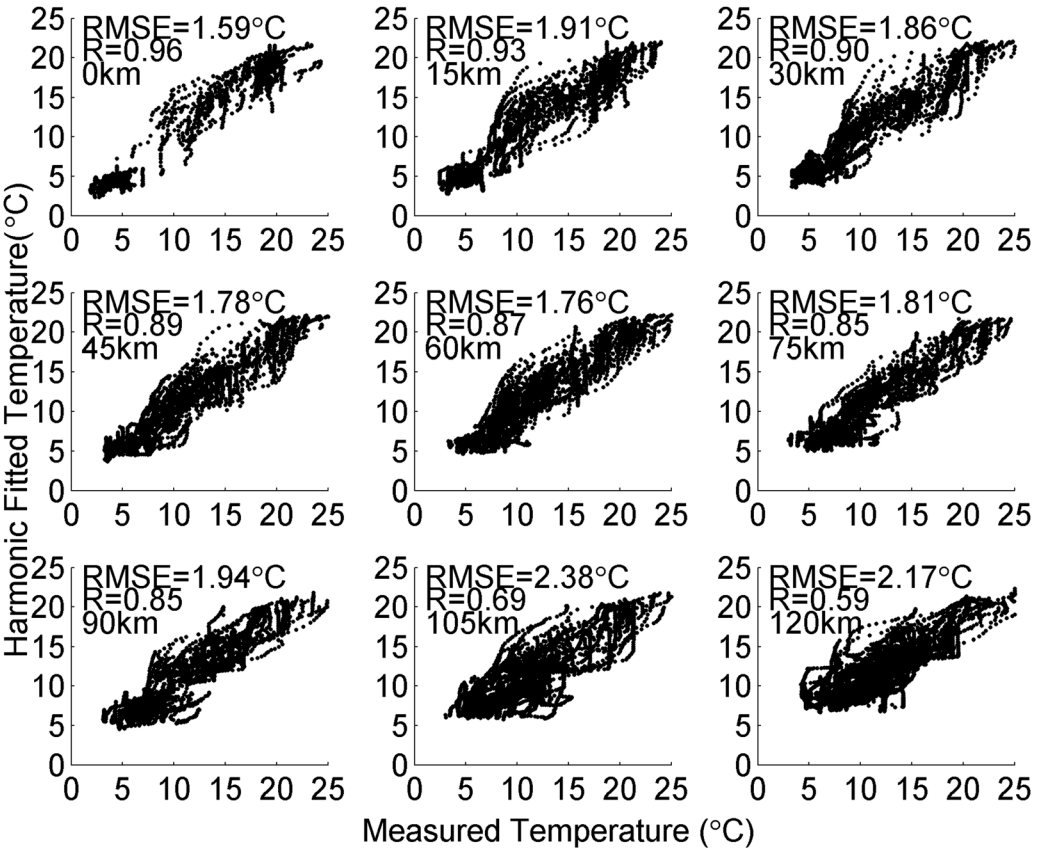

Figure 2. Temperature from harmonic fitting versus measured temperature at different offshore distance (0–120 km). Shown in each plot are the root-mean-square error (RMSE) and the correlation coefficients with $p < 0.05$.

2.4. Steric Height Estimation

There have been discussions on different components contributing to the sea surface height variation in open oceans [*Gill and Niller*, 1973; *Fu and Davidson*, 1995; *Stammer*, 1997; *Vivier et al*., 1999; *Yan et al*., 2004, 2006]. Most are basin scale where the influence of the thermal field is dominant [e.g., *Yan et al*., 2006]. Our essential interests are regions of the continental shelf and slope where the influences of freshwater and the sloping topography need to be assessed. The discussion on the determination of velocities on the shelf and the reconstruction of coastal sea levels has a long history [*Bingham and Hughes*, 2012; *Csanady*, 1979, 1997; *Sheng and Thompson*, 1996; Helland-Hansen, 1934]. In a right-handed coordinate system with positive z vertically up, x offshore direction along the transect, and y alongshore direction perpendicular to the transect, the barometrically corrected sea level anomaly [*Gill and Niller*, 1973] can be expressed as

$$\eta'_{Alt} = \eta'_{steric} + p'_b/\rho_0 g \tag{2}$$

where the steric height anomaly

$$\eta'_{steric} = \int_{-H(x,y)}^{0} [\varepsilon(x,y,z,t) - \bar{\varepsilon}(x,y,z)]\rho_0 dz \tag{3}$$

and $H(x,y)$ is the water depth, p'_b is the time variable part of bottom pressure, ρ_0 is a representative seawater density (a constant), ε is the density defect

$$\varepsilon = \rho(x,y,z,t)^{-1} - {\rho_0}^{-1} \approx \frac{\rho_0 - \rho(x,y,z,t)}{{\rho_0}^2} \tag{4}$$

and $\bar{\varepsilon}$ is the corresponding temporal mean. Furthermore, the steric height deviation is decomposed into the contribution of temperature and salinity, as

$$\eta'_{steric} = \eta'_T + \eta'_S$$
$$= \int_{-H(x,y)}^{0} \alpha[T(x,y,z,t) - \bar{T}(x,y,z)]dz - \int_{-H(x,y)}^{0} \beta[S(x,y,z,t) - \bar{S}(x,y,z)]dz \quad (5)$$
$$= \int_{-H(x,y)}^{0} \alpha T' dz - \int_{-H(x,y)}^{0} \beta S' dz$$

with the thermal and haline expansion coefficients

$$\alpha(x,y,z,t) = -\frac{1}{\rho_0}\frac{\partial \rho}{\partial T} \quad (6)$$

$$\beta(x,y,z,t) = \frac{1}{\rho_0}\frac{\partial \rho}{\partial S} \quad (7)$$

$\bar{T}$ and $\bar{S}$ are the temporal mean of the T and S at each location. Moreover, we are concerned as well with the steric height difference between two locations. Taking the horizontal gradient (∇) of equation (3) in the x-z plane, gives

$$\frac{\partial \eta'_{steric}}{\partial x} = \frac{1}{\rho_0}\int_{-H}^{0} \frac{\partial \rho'}{\partial x} dz + \frac{\rho'_b}{\rho_0}\frac{\partial H}{\partial x} \quad (8)$$

and ρ'_b is the density variation over the seafloor in the offshore direction. The steric height difference is the sum of two parts. The first term on the right of equation (8) is the contribution of horizontal density gradient, and the second term is the influence of the bottom density along the varying topography. The second term is generated because we integrate the steric height over varying water depths. In the open ocean, a common reference level assumed with no geostrophic flow (say 3000 m depth) is chosen, thus the second term is negligible. For the continental shelf and slope, the first term decreases as the decreasing water depth and the second term cannot be neglected. For coastal areas where tidal gauges locate, the contribution from the first term almost vanishes, leaving only the contribution from bottom density and topography [*Bingham and Hughes*, 2012]. The integration of the second term over the x direction can be considered as a correction under the assumption of no geostrophic flow on the seafloor by extending isopycnals horizontally under the seafloor [Helland-Hansen, 1934; *Sheng and Thompson*, 1996] to address the calculated steric height over the sloping bottom, and give the "topography-corrected" steric height at location x_1 with water depth $-H_1$ referring to location x_0 with a common water depth $-H_0$

$$\eta'_{TC} = \int_{-H_1}^{0} \alpha T'(x,y,z,t)dz - \int_{-x_0}^{-x_1} \alpha T'_b \frac{\partial H}{\partial x} dx \quad (9)$$

$$\eta'_{SC} = -\int_{-H_1}^{0} \beta S'(x,y,z,t)dz + \int_{-x_0}^{-x_1} \beta S'_b \frac{\partial H}{\partial x} dx \quad (10)$$

The above equations are equivalent to the steric setup adopted by *Csan*ady [1979] that the path of integration is first along the seafloor from a reference depth to a given location then vertically up to the surface. The topography correction term, as pointed out by *Bingham and Hug*hes [2012], is considered as an approximation to the bottom stress.

3. Temperature and Salinity Annual Cycles

The annual cycles of temperature and salinity were obtained using the method described in section 2.2. In the thermal field (Figure 3a), the surface temperature shows strong seasonal pattern related to the annual heat flux cycle. The water column is well mixed in winter, and highly stratified in summer. The persistence of the cold bottom water at the middle shelf forms the cold pool in the process of stratification from April, and is gradually eroded as thermocline deepens around October and November. Besides the temperature difference within the same month, we also noticed different phases in the cycle (Figure 3b). The middle shelf surface layer water, at 10 m depth with 60 km offshore distance, reaches its peak in August. Whereas the bottom water gains highest temperature in October. The largest vertical temperature difference on the middle shelf occurs in August (~12°C). Our annual

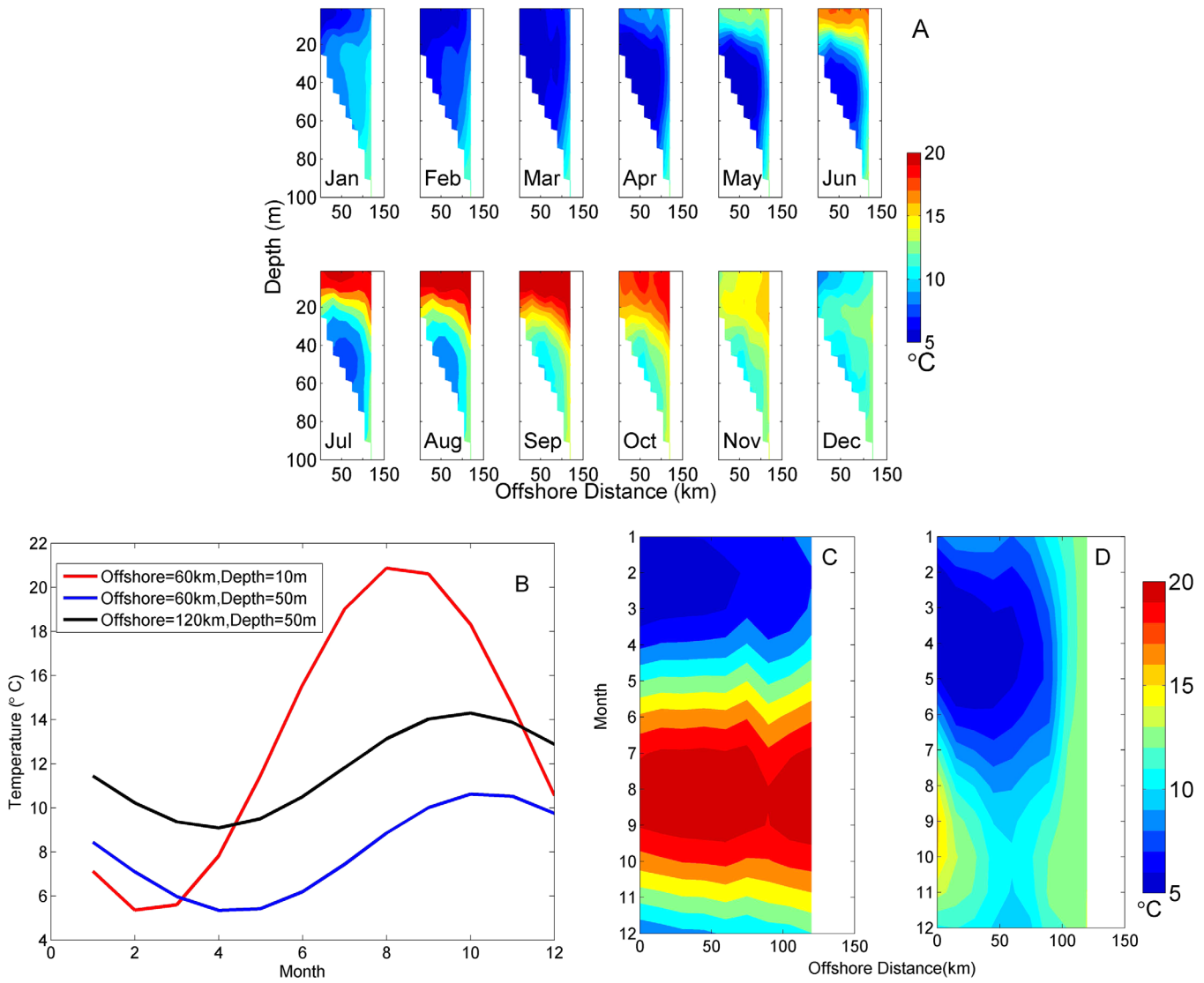

Figure 3. Temperature annual cycles along the transect. (a) Cross-section view of temperature (contour) in different months. (b) Temperature annual cycles at three locations: middle shelf surface (offshore distance = 60 km, depth = 10 m), middle shelf bottom (offshore distance = 60 km, depth = 50 m), and outer shelf bottom (offshore distance = 120 km, depth = 50 m). (c) Surface layer temperature annual evolution. (d) Bottom temperature annual evolution.

fitted temperature distribution show consistent pattern with one recent study [*Forsyth et al.*, 2015] using the Oleander XBTs cross the shelf at a nearby location. The temporal evolution of the bottom temperature (Figure 3c) indicates the location of the cold pool water from April to September in the middle shelf.

In the salinity field (Figure 4a), the dominant feature is the nearshore and near-surface freshwater from the shelf flow and local rivers [*Fairbanks*, 1982; *Chapman et al.*, 1986; *Chapman and Beardsley*, 1989], with the summer offshore surface-advection and dispersion [*Yankovsky and Chapman*, 1997; *Sanders and Garvine*, 2001]. The surface and bottom salinity in the middle shelf are showing same pace leading the outer shelf (Figure 4b), which are probably related to the freshwater advection from the mean flow upstream. For the bottom salinity, there is a steady salinity gradient from the coast to the outer shelf through all the season. Although the cold pool is sharing the same boundary in both thermal and haline fields with the slope water (shelf break front), the cold pool pattern is found mainly only in the thermal field. Thus, we consider the surface expression of the cold pool, if it exists, comes from the thermal field.

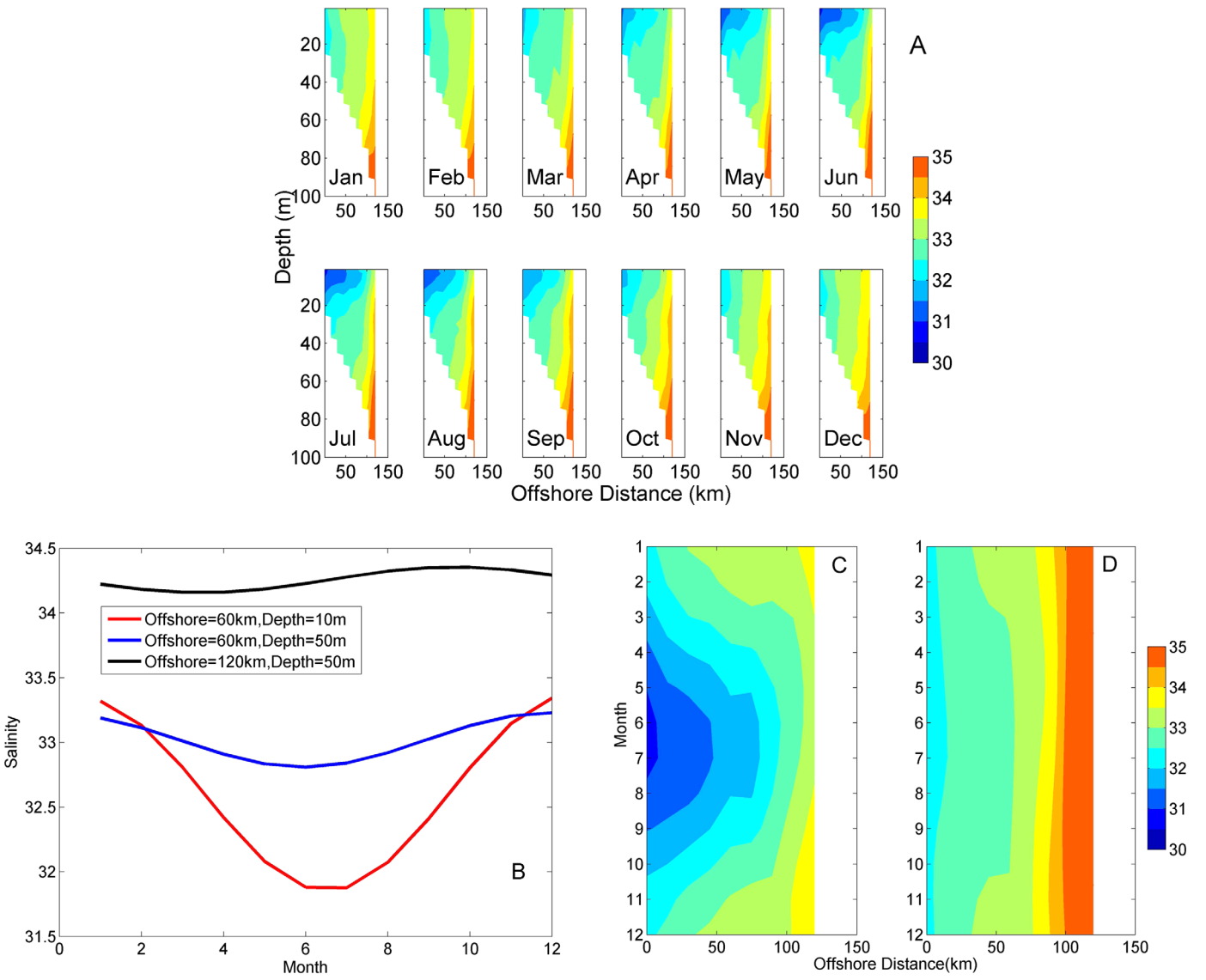

Figure 4. Salinity annual cycles along the transect. (a) Cross-section view of salinity in different months. (b) Salinity annual cycles at three locations: middle shelf surface (offshore distance = 100 km, depth = 10 m), middle shelf bottom (offshore distance = 100 km, depth = 50 m), and outer shelf bottom (offshore distance = 160 km, depth = 50 m). (c) Surface layer salinity annual evolution. (d) Bottom salinity annual evolution.

4. Derived Steric Components

The topography-corrected thermal steric height variation (Figure 5a) is derived as section 2.4. Lower temperature generates depressed thermal steric height. Temporally, the thermal steric height is high in summer and low in winter, being consistent with the distribution of surface water temperature (Figure 3c), and thus is mostly controlled by the seasonal cycle of heat flux. A "wedge" pattern is remarkable with depressed height in the middle shelf around 50 km offshore distance spanning from May to September, which colocates with the cold pool revealed in the bottom temperature (Figure 3d). The forming of this wedge is possibly explained by the retention of the cold water in the middle shelf.

The salinity presents a seasonal pattern as well with lower haline steric height during the spring and summer (Figure 4c). Moreover, the distribution of the haline steric height presents an elevated height in the middle shelf comparing with the inner and outer shelf, which is opposite to the "wedge" pattern in the thermal steric height distribution. Thus, the haline pattern compensates the imprints of the thermal feature of the cold pool when further considering the total steric height. However, within the annual cycle

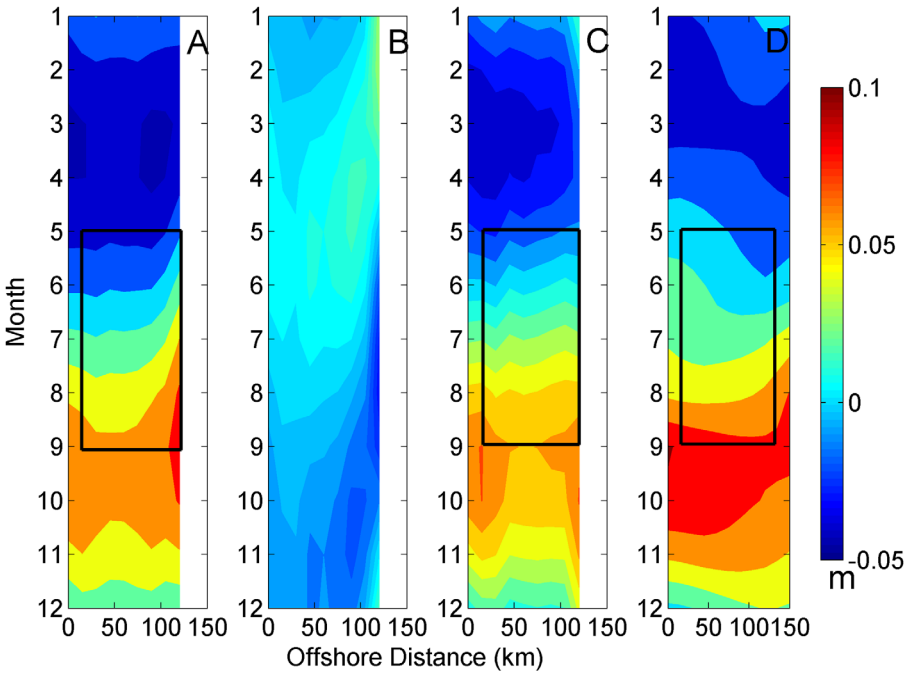

Figure 5. Annual evolution (contour) of different steric components and the monthly climatological altimetry SLA. From left to right: (a) thermal steric height, (b) haline steric height, (c) total steric height, and (d) averaged altimetry SLA. The total steric height is the sum of thermal and haline steric components. The black rectangles in Figures 5a, 5c, and 5d are the central depressed pattern colocating with the cold pool.

(Figure 6), the thermal steric height ranges from −0.04 m to 0.09 m, while the haline steric height ranges from −0.03 to 0.02 m. The lowest haline steric height and highest thermal steric height in summer (say, August) comes from shelf break front, related to the shelf/slope water exchange [*Chapman et al.*, 1986; *Fairbanks*, 1982; *Csanady and Hamilton*, 1988]. In the shelf, the haline steric height varies much less than the thermal steric height. Concerning the magnitude in each month, the thermal steric height is smaller than the haline steric height during May and June, suggesting that during these months the thermal features could be damped by the salinity distribution. While in July and August, especially the latter month, the thermal steric plays a major role in the total steric height (Figure 5c). Moreover, the retrieved thermal steric height is also compared to the altimetry SLA, which is the 20 year averaged mean SLA annual cycle, with R^2=0.87 suggesting that the thermal steric height explains 87% variation of the SLA (Figure 7). Considering this is a spatial-temporal comparison including all the transect locations, the high correlation coefficient between the thermal steric height and SLA indicates that these two variables are not only roughly temporally in phase but also spatially coherent. The cold pool feature, which exists in the thermal field with the depressed height in the middle shelf, can also be found in the SLA especially during July and August when the thermal steric height is much larger than the haline steric height.

5. EEMD and the Application

As analyzed in previous sections, the cold pool feature is found in the 20 year mean altimetry SLA (Figure 5d). The altimetry SLA is the combination of components of different time scales, containing oscillations with spectrum ranging from one cycle per month to interannual. These components are damped out in the process of taking the 20 year average. One remaining question is whether and how the cold pool feature could be found from single-year altimetry data. Taking the year 2010 (Figure 8a) as an example, short time scale (1–2 months) disturbances are mixed with the cold pool feature, causing the sea level anomaly to be elevated (March and November) or depressed (July), and making the cold pool identification impossible. As the cold pool is an annual signal, we employ EEMD (section 2.3) to decompose the SLA data into different frequency components and extract components with dominating annual signals to reconstruct the

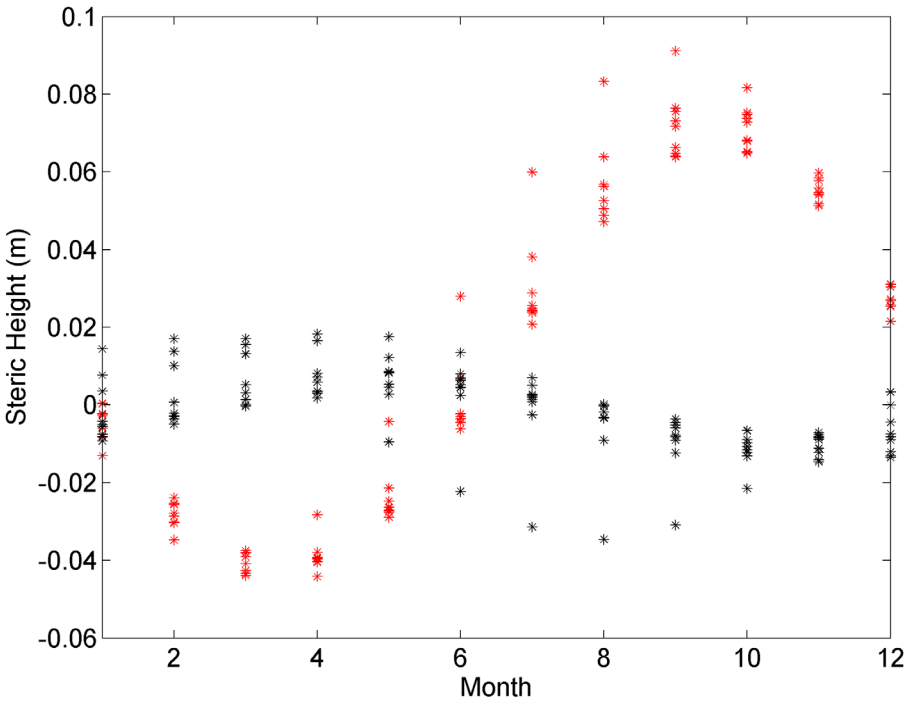

Figure 6. The comparison between the thermal steric height (red stars) and haline steric height (black stars) annual cycle.

SLA field. Figure 8b shows the reconstructed SLA of 2010, which is one of many years that the middle shelf depressed height can be found in the reconstructed SLA.

Furthermore, the locations of SLA middle-shelf depression in the cross-shelf direction are identified year by year. Correspondingly, the cold core location can also be determined from in situ measurements for those years with enough TS profiles (Figure 9). Temperature profiles from XBT and MBT are included for better spatial and temporal coverage. The location uncertainty of in situ measurements is determined by the transect offshore resolution (15 km), while the locations of SLA depression have an uncertainty around 25 km considering both the original SLA 0.25° resolution (22.2 km × 21.3 km at 40°N) and the inclined angle of the transect. We found general agreement between the SLA depression and the cold core locations. The cold core locations coincide with the SLA depression locations in 1993 and 1996. For the years 1994, 2002, 2003, 2004, and 2009, the cold core locations are next to the SLA trough location within the uncertainty range. The interannual variation of the SLA depression locations shows consistent pattern with the cold core locations during 1993–1996 and 2002–2004. These results suggest a promising application of the SLA data indicating the location of the cold pool. It should be noted that the SLA data within 25 km offshore are subjected to land contamination, thus the identified results should be treated with caution (e.g., the year 2007).

6. Discussion

This study investigated the relationship between the cross-shelf sea level variation and the cold pool in the Middle Atlantic Bight for the first time. The persistence of the cold pool water generates depressed thermal steric height in the middle shelf. Colocated depression features are found in the annual evolution of the thermal steric height, total steric height, and satellite observed SLA. The modulation of the sea level variations by the cold pool is revealed that the small variation induced by the cold pool overlies with the major seasonal cycle dominated by the solar heat flux. This study provides insights into the composition of the sea level variations on the continental shelf, and thus contributes to the understanding of the response of the sea level variations to mesoscale water masses on the continental shelf.

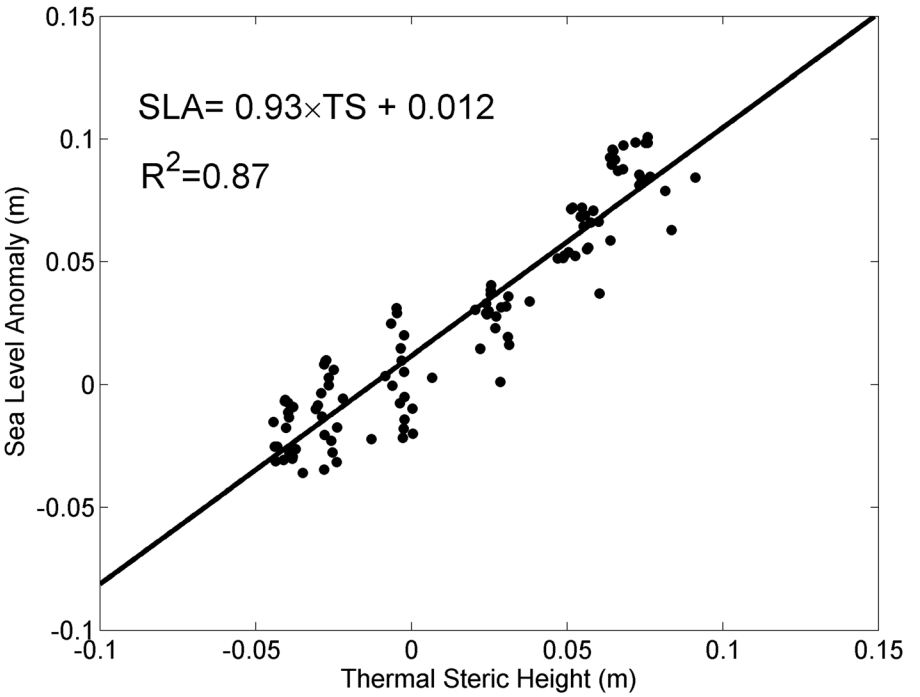

Figure 7. Derived thermal steric height versus altimetry SLA. The black line indicates the linear fitting.

Concerning the altimeter accuracy, the uncertainty of altimetry SLA is about 2 cm [*Cheney et al.*, 1994] . In this study, the altimetry data is averaged over 20 years with the standard error of the mean around 5 mm (in August) as shown in Figure 10. The bottom temperature difference between 45 km offshore and 120 km offshore is around 4°C. The estimated thermal steric height over the same offshore distance is about 3.6 cm. The corresponding SLA difference is approximately 1.2 cm but the sea level difference increases consistently by

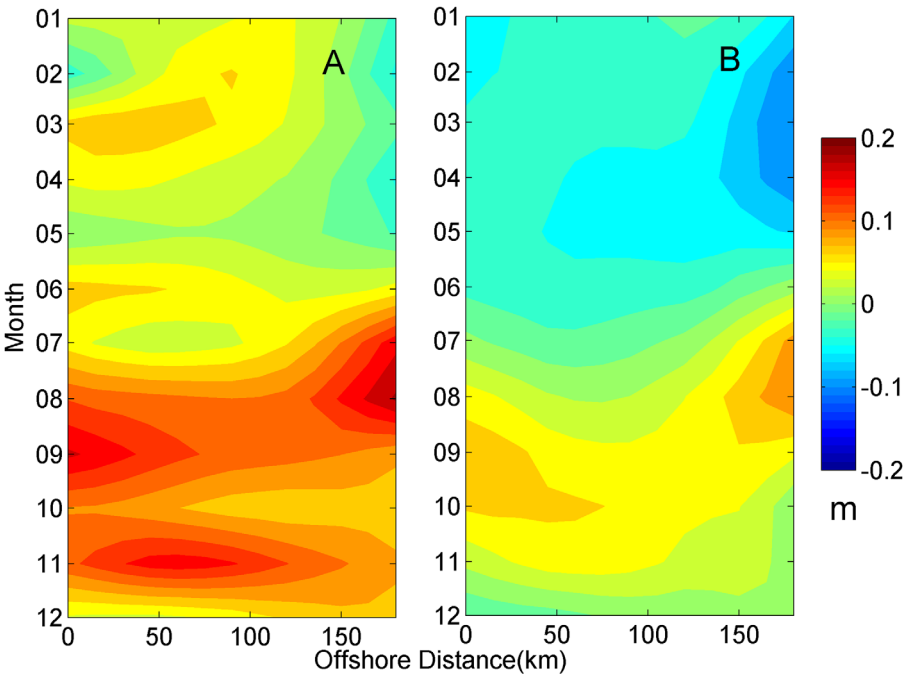

Figure 8. Comparison of (a) altimetry SLA and (b) the seasonal components using EEMD in 2010.

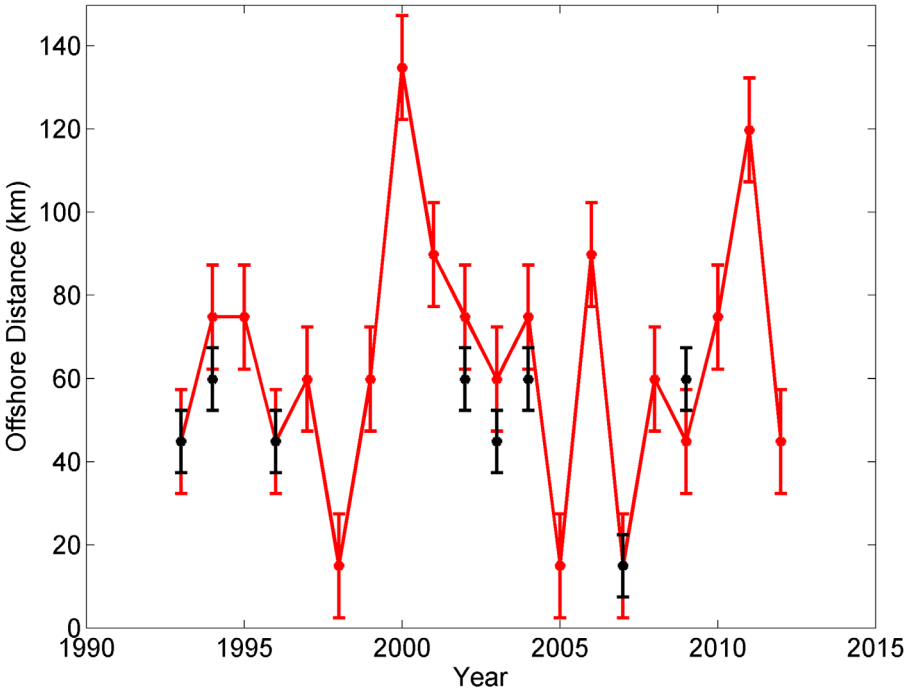

Figure 9. The location comparison in the offshore direction. The red dots are the locations of altimetry SLA depression, and the black dots are the locations of the cold core identified from in situ measurements.

3 cm at 150 km offshore and 5–6 cm at 180 km offshore. Thus, the coherent pattern in the altimetry SLA data is not within the error bounds.

The contribution from the salinity field is investigated. The freshwater forms a narrow near-surface band (Figure 4), expanding offshore in the surface layer in the summer time [*Chapman et al.*, 1986]. The annual

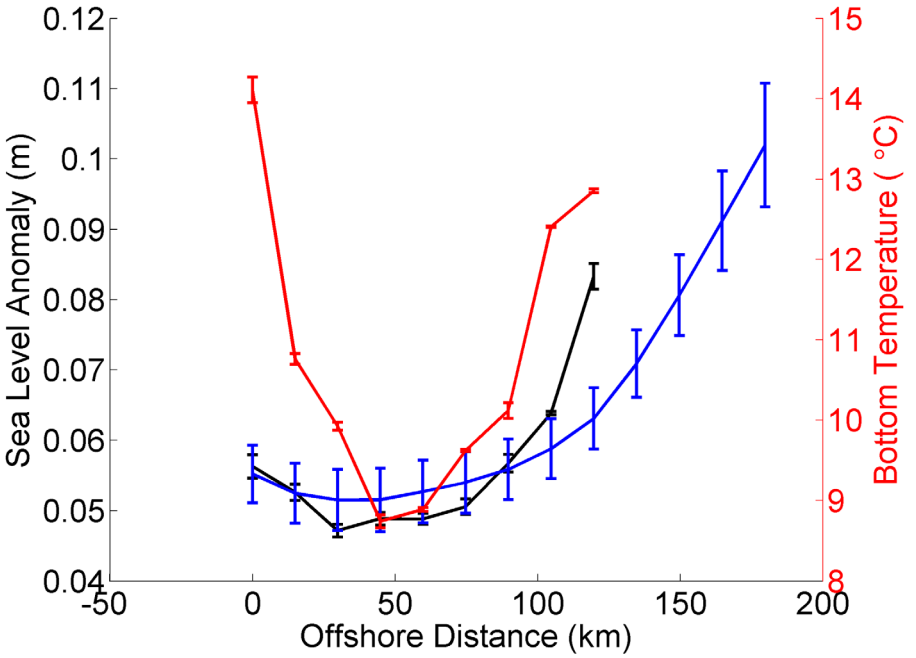

Figure 10. Comparison between the bottom temperature, corrected thermal steric height, and altimeter SLA in August. The red line is the bottom temperature, black line is the derived thermal steric height, and the blue line is the SLA from altimeter. The error bar for each curve denotes the standard error of the mean.

variation of the haline steric height is much smaller than that of the thermal steric height (Figure 6), which explains the high correlation between the thermal steric height and the SLA (Figure 7). Concerning the magnitude of the haline and thermal steric heights in specific months, the haline steric height is of the same magnitude in the early summer (around June). This explains why cold pool features forms from May (Figure 3a) but the middle shelf depressed height is found after June, especially in August, in SLA (Figure 5). It should be noted that the influence of the haline field is location specified. We also made transects downstream (figures are not shown here), which passes through the transport pathways of the Hudson River [*Chant et al*., 2008; *Zhang et al*., 2009]. The annual variations of the haline steric height along those transects are of the same magnitude as the thermal steric height, and the squared correlation coefficients between the thermal steric height and SLA decreases correspondingly.

Processes of different temporal and spatial scales such as wind forcing [*Li et al*., 2014] could also influence the sloping sea level. Our primary interest is the influence of the cold pool, which occurs as one cycle per year. Thus, we focus on the annual cycle of temperature and salinity, and adopt several data processing methods to eliminate oscillation signals of other time scales. The single annual harmonic fitting is applied to the TS profiles, and the fitted results are averaged over 20 years together with the SLA data. EEMD, which can extract both seasonal and interannual variability from nonstationary signals, is not applicable to the TS profiles because the in situ measurements are not continuous. Moreover, the influence of the cold pool to the thermal steric height and SLA is considered as a static effect (thermal expansion) in this study although the sea surface slope and cross-shelf density gradients are associated with an along-shelf geostrophic flow. Under our data processing steps (harmonic fitting, 20 year average and EEMD), the thermal steric height explains 87% variations of SLA. The dynamic processes including wind and waves could still contribute to the sea surface slope but are out of the scope of this study.

Our study investigates the cold pool modulation to the sea level slope and builds up a relationship between them. EEMD is applied to altimetry SLA to extract the annual cycle components so that the middle shelf depression can be found for single year's data without average. The locations of SLA depression (Figure 9) are consistent with the in situ cold core locations, suggesting the linkage between these two variables and a promising application of altimetry SLA to the cold pool study, despite large uncertainties due to the sparse of the in situ measurements, SLA resolutions, and coastal SLA errors. We noticed the locations of both the cold pool and SLA depressions show an agreement with the variation of the Labrador Current (LC) transport [*Han et al*., 2010]: during the period 1993–1996, the Labrador Current transport anomalies first increased then decreased along with NAO index, while the cold pool locations moved offshore and then onshore. Similar pattern also occurred during 2002–2004. In the year 2000, the SLA trough moved further offshore around 140 km, while the LC transport is not available but NAO index peaked. The cold pool variations are subjected to further investigation, but the linkage with LC transport and NAO are possible recalling that the cold pool water is the retention of the cold shelf water coming from further north [*Fairbanks*, 1982; *Chapman et al*., 1986; *Shearman and Lentz*, 2009].

Acknowledgments

The in situ measurements of CTD, PFL, XBT, and MBT can be obtained from World Ocean Database/NODC/NOAA (http://www.nodc.noaa.gov/OC5/SELECT/dbsearch/dbsearch.html). The gridded SLA data are Ssalto/Duacs multimission altimeter products from AVISO/CNES (http://www.aviso.oceanobs.com/en/data/products/sea-surface-height-products/global/msla). This research benefitted from comments of Steven Lentz (WHOI). The authors also thank Autumn Kidwell for the proofreading. The first author, Jin Sha, is supported partially by the fellowship from China Scholarship Council. The research of this work is supported by the NOAA Sea grant (Na14OAR4170087).

References

Bigelow, H. B. (1933), Studies of the waters on the continental shelf, Cape Cod to Chesapeake Bay. I. The cycle of temperature, *Pap. Phys. Oceanogr. Meteorol.*, *2*, 1–35.

Bignami, F., and T. S. Hopkins (2003), Salt and heat trends in the shelf waters of the southern Middle-Atlantic Bight, *Cont. Shelf Res.*, *23*(6), 647–667, doi:10.1016/S0278-4343(03)00023-2.

Bingham, R. J., and C. W. Hughes (2012), Local diagnostics to estimate density-induced sea level variations over topography and along coastlines, *J. Geophys. Res.*, *117*, C01013, doi:10.1029/2011JC007276.

Chant, R., et al. (2008), Dispersal of the Hudson River plume in the New York Bight: Synthesis of observational and numerical studies during LaTTE, *Oceanography*, *21*(4), 148–161.

Chapman, D. C., and R. C. Beardsley (1989), On the origin of shelf water in the Middle Atlantic Bight, *J. Phys. Oceanogr.*, *19*(3), 384–391, doi:10.1175/1520-0485(1989)019<0384:OTOOSW>2.0.CO;2.

Chapman, D. C., J. A. Barth, R. C. Beardsley, and R. G. Fairbanks (1986), On the continuity of mean flow between the Scotian Shelf and the Middle Atlantic Bight, *J. Phys. Oceanogr.*, *16*(4), 758–772, doi:10.1175/1520-0485(1986)016<0758:OTCOMF>2.0.CO;2.

Cheney, R., L. Miller, R. Agreen, N. Doyle, and J. Lillibridge (1994), TOPEX/POSEIDON: The 2-cm solution, *J. Geophys. Res.*, *99*(C12), 24,555–24,563, doi:10.1029/94JC02050.

Churchill, J. H., and G. G. Gawarkiewicz (2014), Shelf water and chlorophyll export from the Hatteras slope and outer shelf, *J. Geophys. Res. Oceans*, *119*, 4291–4304, doi:10.1002/2014JC009809.

Csanady, G. T. (1979), The pressure field along the western margin of the North Atlantic, *J. Geophys. Res.*, *84*(C8), 4905–4915, doi:10.1029/JC084iC08p04905.

Csanady, G. T. (1982), *Circulation in the Coastal Ocean*, Springer, Netherlands, doi:10.1007/978-94-017-1041-1.

Csanady, G. T. (1997), On the theories that underlie our understanding of continental shelf circulation, *J. Oceanogr.*, *53*, 207–230.
Csanady, G. T., and P. Hamilton (1988), Circulation of slopewater, *Cont. Shelf Res.*, *8*(5–7), 565–624, doi:10.1016/0278-4343(88)90068-4.
Fairbanks, R. G. (1982), The origin of continental shelf and slope water in the New York Bight and Gulf of Maine: Evidence from $H_2^{18}O/H_2^{16}O$ ratio measurements, *J. Geophys. Res.*, *87*(C8), 5796–5808, doi:10.1029/JC087iC08p05796.
Forsyth, J., M. Andres, and G. G. Gawarkiewicz (2015), Recent accelerated warming of the continental shelf off New Jersey: Observations from the CMV Oleander XBT line, *J. Geophys. Res. Oceans*, *120*, 2370–2384, doi:10.1002/2014JC010516.
Fu, L.-L., and R. A. Davidson (1995), A note on the barotropic response of sea level to time-dependent wind forcing, *J. Geophys. Res.*, *100*(C12), 24,955–24,963, doi:10.1029/95JC02259.
Gill, A. E., and P. P. Niller (1973), The theory of the seasonal variability in the ocean, *Deep Sea Res. Oceanogr. Abstr.*, *20*(2), 141–177, doi:10.1016/0011-7471(73)90049-1.
Han, G., K. Ohashi, N. Chen, P. G. Myers, N. Nunes, and J. Fischer (2010), Decline and partial rebound of the Labrador Current 1993–2004: Monitoring ocean currents from altimetric and conductivity-temperature-depth data, *J. Geophys. Res.*, *115*, C12012, doi:10.1029/2009JC006091.
Helland-Hansen, B. (1934), The Sognefjord section: Oceanographic Observations in the northernmost part of the North Sea and the southern part of the Norwegian Sea, in *James Johnstone Memorial Volume*, pp. 257–274, Liverpool Univ. Press, Liverpool, U. K.
Houghton, R. W., R. Schlitz, R. C. Beardsley, B. Butman, and J. L. Chamberlin (1982), The Middle Atlantic Bight cold pool: Evolution of the temperature structure during summer 1979, *J. Phys. Oceanogr.*, *12*(10), 1019–1029, doi:10.1175/1520-0485(1982)012<1019:TMABCP>2.0.CO;2.
Huang, N. E., Z. Shen, S. R. Long, M. C. Wu, H. H. Shih, Q. Zheng, N.-C. Yen, C. C. Tung, and H. H. Liu (1998), The empirical mode decomposition and the Hilbert spectrum for nonlinear and non-stationary time series analysis, *Proc. R. Soc. London, Ser. A*, *454*(1971), 903–995, doi:10.1098/rspa.1998.0193.
Ienna, F., Y.-H. Jo, and X.-H. Yan (2014), A new method for tracking meddies by satellite altimetry, *J. Atmos. Oceanic Technol.*, *31*(6), 1434–1445, doi:10.1175/JTECH-D-13-00080.1.
Ketchum, B. H., and N. Corwin (1964), The persistence of "winter" water on the continental shelf south of Long Island, New York, *Limnol. Oceanogr.*, *9*(4), 467–475, doi:10.4319/lo.1964.9.4.0467.
Klemas, V., and X.-H. Yan (2014), Subsurface and deeper ocean remote sensing from satellites: An overview and new results, *Prog. Oceanogr.*, *122*, 1–9, doi:10.1016/j.pocean.2013.11.010.
Lentz, S. J. (2003), A climatology of salty intrusions over the continental shelf from Georges Bank to Cape Hatteras, *J. Geophys. Res.*, *108*(C10), 3326, doi:10.1029/2003JC001859.
Lentz, S. J. (2008), Seasonal variations in the circulation over the Middle Atlantic Bight continental shelf, *J. Phys. Oceanogr.*, *38*(7), 1486–1500, doi:10.1175/2007JPO3767.1.
Lentz, S. J., B. Butman, and C. Harris (2014), The vertical structure of the circulation and dynamics in Hudson Shelf Valley, *J. Geophys. Res. Oceans*, *119*, 3694–3713, doi:10.1002/2014JC009883.
Li, Y., R. Ji, P. S. Fratantoni, C. Chen, J. A. Hare, C. S. Davis, and R. C. Beardsley (2014), Wind-induced interannual variability of sea level slope, along-shelf flow, and surface salinity on the Northwest Atlantic shelf, *J. Geophys. Res. Oceans*, *119*, 2462–2479, doi:10.1002/2013JC009385.
Malone, T. C., T. S. Hopkins, P. G. Falkowski, and T. E. Whitledge (1983), Production and transport of phytoplankton biomass over the continental shelf of the New York bight, *Cont. Shelf Res.*, *1*(4), 305–337, doi:10.1016/0278-4343(83)90001-8.
Narváez, D. A., D. M. Munroe, E. E. Hofmann, J. M. Klinck, E. N. Powell, R. Mann, and E. Curchitser (2014), Long-term dynamics in Atlantic surfclam (*Spisula solidissima*) populations: The role of bottom water temperature, *J. Mar. Syst.*, *141*, 136–148, doi:10.1016/j.jmarsys.2014.08.007.
Sanders, T. M., and R. W. Garvine (2001), Fresh water delivery to the continental shelf and subsequent mixing: An observational study, *J. Geophys. Res.*, *106*(C11), 27,087–27,101, doi:10.1029/2001JC000802.
Shearman, R. K., and S. J. Lentz (2009), Long-term sea surface temperature variability along the U.S. East Coast, *J. Phys. Oceanogr.*, *40*(5), 1004–1017, doi:10.1175/2009JPO4300.1.
Sheng, J., and K. R. Thompson (1996), A robust method for diagnosing regional shelf circulation from scattered density profiles, *J. Geophys. Res.*, *101*(C11), 25,647–25,659, doi:10.1029/96JC01331.
Stammer, D. (1997), Steric and wind-induced changes in TOPEX/POSEIDON large-scale sea surface topography observations, *J. Geophys. Res.*, *102*(C9), 20,987–21,009, doi:10.1029/97JC01475.
Sullivan, M. C., R. K. Cowen, and B. P. Steves (2005), Evidence for atmosphere–ocean forcing of yellowtail flounder (*Limanda ferruginea*) recruitment in the Middle Atlantic Bight, *Fish. Oceanogr.*, *14*(5), 386–399, doi:10.1111/j.1365-2419.2005.00343.x.
Vivier, F., K. A. Kelly, and L. Thompson (1999), Contributions of wind forcing, waves, and surface heating to sea surface height observations in the Pacific Ocean, *J. Geophys. Res.*, *104*(C9), 20,767–20,788, doi:10.1029/1999JC900096.
Wood, A. M., N. D. Sherry, and A. Huyer (1996), Mixing of chlorophyll from the Middle Atlantic Bight cold pool into the Gulf Stream at Cape Hatteras in July 1993, *J. Geophys. Res.*, *101*(C9), 20,579–20,593, doi:10.1029/96JC01135.
Wu, Z., and N. E. Huang (2009), Ensemble empirical mode decomposition: A noise-assisted data analysis method, *Adv. Adaptive Data Anal.*, *01*(01), 1–41, doi:10.1142/S1793536909000047.
Wu, Z., N. E. Huang, and X. Chen (2009), The multi-dimensional ensemble empirical mode decomposition method, *Adv. Adaptive Data Anal.*, *01*(03), 339–372, doi:10.1142/S1793536909000187.
Yan, X.-H., J. Pan, Y.-H. Jo, M.-X. He, W. T. Liu, and L. Jiang (2004), Role of winds in estimation of ocean heat storage anomaly using satellite data, *J. Geophys. Res.*, *109*, C03041, doi:10.1029/2003JC002202.
Yan, X.-H., Y.-H. Jo, W. T. Liu, and M.-X. He (2006), A new study of the Mediterranean outflow, air–sea interactions, and meddies using multisensor data, *J. Phys. Oceanogr.*, *36*(4), 691–710, doi:10.1175/JPO2873.1.
Yankovsky, A. E., and D. C. Chapman (1997), A simple theory for the fate of buoyant coastal discharges, *J. Phys. Oceanogr.*, *27*(7), 1386–1401, doi:10.1175/1520-0485(1997)027<1386:ASTFTF>2.0.CO;2.
Zhang, W. G., J. L. Wilkin, and R. J. Chant (2009), Modeling the pathways and mean dynamics of river plume dispersal in the New York Bight, *J. Phys. Oceanogr.*, *39*(5), 1167–1183, doi:10.1175/2008JPO4082.1.